ADVANCED MATERIALS
www.advmat.de

11.2% All-Polymer Tandem Solar Cells with Simultaneously Improved Efficiency and Stability

Kai Zhang, Ruoxi Xia, Baobing Fan, Xiang Liu, Zhenfeng Wang, Sheng Dong, Hin-Lap Yip, Lei Ying, Fei Huang,* and Yong Cao*

All-polymer solar cells (all-PSCs) that contain both p-type and n-type polymeric materials blended together as light-absorption layers have attracted much attention, since the blend of a polymeric donor and acceptor should present superior photochemical, thermal, and mechanical stability to those of small molecular-based organic solar cells. In this work, the interfacial stability is studied by using highly stable all-polymer solar cell as a platform. It is found that the thermally deposited metal electrode atoms can diffuse into the active layer during device storage, which consequently greatly decreases the power conversion efficiency. Fortunately, the diffusion of metal atoms can be slowed down and even blocked by using thicker interlayer materials, high-glass-transition-temperature interlayer materials, or a tandem device structure. Learning from this, homojunction tandem all-PSCs are successfully developed that simultaneously exhibit a record power conversion efficiency over 11% and remarkable stability with efficiency retaining 93% of the initial value after thermally aging at 80 °C for 1000 h.

Polymer solar cells (PSCs) composed of organic semiconductors have been extensively investigated, leading to dramatically improved overall photovoltaic performance in recent years.[1] Compared to thin-film inorganic solar cells, PSCs have specific advantages of solution processability, light weight, good mechanical flexibility, and low cost, making themselves a potential candidate for flexible and wearable devices application.[2–4] The prerequisites to fabricate high-performance PSCs for practical applications include high power conversion efficiencies (PCEs) and good stability. Much effort has been devoted to improving PCEs by designing and synthesizing new donor/acceptor materials and interfacial materials, optimizing the morphology of bulk-heterojunction films, adopting new device architectures, and so forth[5–10]; yet, less attention has been paid to improve the long-term stability of these devices.

Dr. K. Zhang, R. Xia, B. Fan, X. Liu, Z. Wang, Dr. S. Dong, Prof. H.-L. Yip, Prof. L. Ying, Prof. F. Huang, Prof. Y. Cao
Institute of Polymer Optoelectronic Materials and Devices
State Key Laboratory of Luminescent Materials and Devices
South China University of Technology
Guangzhou 510640, P. R. China
E-mail: msleiying@scut.edu.cn; msfhuang@scut.edu.cn

The ORCID identification number(s) for the author(s) of this article can be found under https://doi.org/10.1002/adma.201803166.

DOI: 10.1002/adma.201803166

Typical polymer solar cells (PSCs) are composed of a light-absorption layer and interfacial layers sandwiched between two electrodes; thus, the stability of both the light-absorption layer and the interfacial layer would affect the overall stability. However, among the reported works on device stability, most studies have focused on the photochemical and morphological stability of light-absorption layers.[11–13] For instance, devices suffer irreversible breakdown of the photovoltaic performance caused by oxygen and water in the presence of light that can lead to photo-oxidation of the light-absorption layer and corrosion of the electrodes.[14,15] However, even though a wide range of interfacial layers have been developed and integrated into highly efficient PSCs,[16–18] studies on the stability of interfacial layers are rarely seen.

All-polymer solar cells (all-PSCs) that contain both p-type and n-type polymeric materials blended together as light-absorption layers have attracted much attention,[19–21] since the blend of a polymeric donor and acceptor should present superior photochemical, thermal, and mechanical stability to those of fullerene-based PSCs. For example, by comparing the thermal and photostabilities of all-PSCs and fullerene-based PSCs based on the same polymer donor, all-PSCs exhibited remarkable thermal and photostabilities, while the power conversion efficiencies (PCEs) of devices based on fullerene derivatives decreased rapidly upon thermal annealing or light illumination.[22–24] More importantly, all-PSCs exhibit dramatically enhanced strength and flexibility in elongation at break and toughness, respectively, compared to those observed from devices based on fullerene derivatives.[25,26] Although all-PSCs exhibited an impressively high efficiency over 9% by rational molecular design and device fabrication optimization,[27–30] the overall performance of all-PSCs still lags behind the outstanding efficiency obtained from devices based on small-molecule non-fullerene acceptors. Thus, it remains high priority to develop all-PSCs with high PCEs while retaining good stability.

In this work, we developed homojunction tandem all-PSCs that simultaneously exhibited a high PCE over 11% and remarkable stability with efficiency retaining 93% of the initial value after thermally aging at 80 °C for 1000 h. The photoactive layer of both front and back cells was composed of an electron-donating polymer

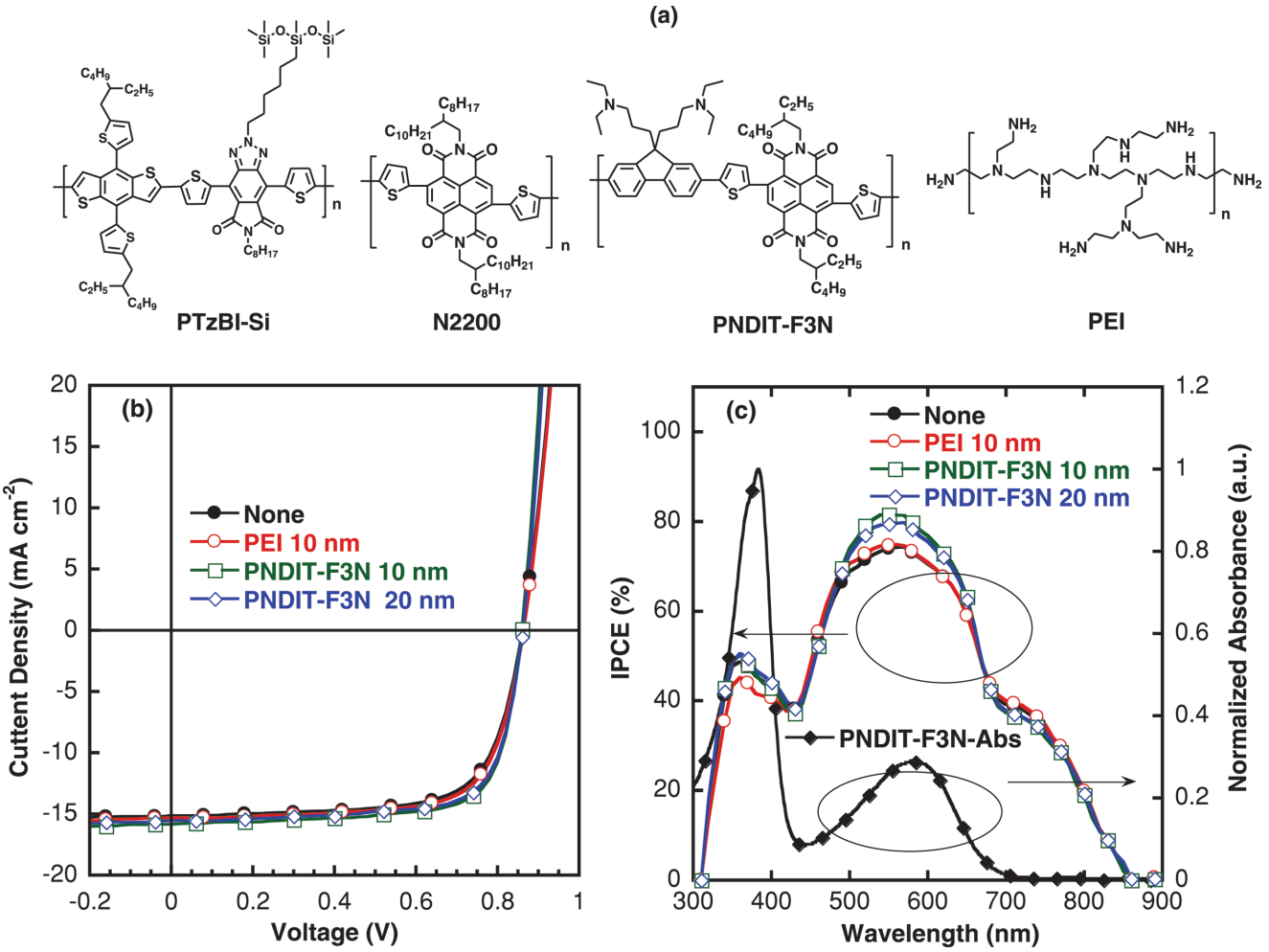

Figure 1. a) Chemical structures of the active layer and interlayer materials used in this study. b) *J–V* and c) EQE characteristics of all-PSCs with different ETLs.

poly{(4,8-bis(5-(2-ethylhexyl)thiophen-2-yl)benzo[1,2-*b*:4,5-*b*′]dithiophene-*co*-4,8-di(thien-2-yl)-2-(6-(1,1,1,3,5,5,5-heptamethyltrisiloxan-3-yl)hexyl)-6-octyl[1,2,3]triazolo[4,5-*f*]isoindole-5,7(2H,6H)-dione} (PTzBI-Si) and an electron-accepting polymer poly[*N*,*N*′-bis(2-octyldodecyl)-naphthalene-1,4,5,8-bis(dicaroximide)-2,6-diyl]-*alt*-5,5′-(2,2′-bithiophene) (with a commercial name of N2200) (**Figure 1**a). The remarkable stability of the resulting homotandem devices can be ascribed to the participation of the incorporated interfacial cathode layer poly[(9,9-bis(3′-(*N*,*N*-dimethylamino)propyl)-2,7-fluorene)-*alt*-5,5′-bis(2,2′-thiophene)-2,6-naphthalene-1,4,5,8-tetracaboxylic-*N*,*N*′-di(2-ethylhexyl)imide] (PNDIT-F3N) in charge dissociation at the interface, which can effectively reduce the diffusion of the metal atoms of electrodes during deposition and storage.

The initial study is carried out by fabricating all-PSCs with the device configuration of indium tin oxide (ITO)/poly(3,4-ethylenedioxythiophene):poly(styrenesulfonate) (PEDOT:PSS)/PTzBI-Si:N2200/ETL/Ag, where poly(ethyleneimine) (PEI, 10 nm), PNDIT-F3N (10 nm), or PNDIT-F3N (20 nm) was used as the electron transport layer (ETL). Here, PEI was utilized because it is an efficient nonconjugated ETL material in fullerene-based PSCs and is widely used.[31,32] A device without an ETL was also fabricated for comparison. The current–density–voltage (*J–V*) curves of devices measured under AM 1.5G irradiation (100 mW cm^{-2}) and the corresponding external quantum efficiency (EQE) spectra are provided in Figure 1b,c. The devices data are summarized in **Table 1**. Interestingly, the all-PSC fabricated without an ETL shows an impressively high PCE of 9.0%, with a short-circuit current density (J_{SC}) of 15.1 mA cm^{-2}, an open-circuit voltage (V_{OC}) of 0.86 V, and a fill factor (FF) of 70%. By inserting a thin layer of PEI (thickness of ≈10 nm), the PCE slightly improved to 9.3% (V_{OC} = 0.86 V, J_{SC} = 15.2 mA cm^{-2}, FF = 71%). Notably, the improvement in PCE is less pronounced than those observed from fullerene-based PSCs with PEI as the interfacial layer.[31] In contrast, devices based on PNDIT-F3N (thickness of ≈10 nm) as the ETL presented an apparently improved PCE of 10% (V_{OC} = 0.86 V, J_{SC} = 15.8 mA cm^{-2}, FF = 73%). The improved PCE is mainly attributed to the enhanced J_{SC}, which can be correlated with the enhanced EQE response in the ranges of 350–420 nm and 500–680 nm. The observed enhanced response regions are consistent with the absorption spectrum of PNDIT-F3N. In this respect, the n-type semi-conductive backbone of PNDIT-F3N acts as an electron acceptor that can combine with the electron-donating

Table 1. Device data for all-PSCs with different ETLs.

ETL	ETL thickness [nm]	Mea. J_{sc} [mA cm^{-2}]	Int. J_{sc} [mA cm^{-2}]	V_{oc} [V]	FF [%]	PCE [avg[a)]/max] [%]
None	0	15.1	14.8	0.86	70	8.6 ± 0.4(9.0)
PEI	10	15.2	14.8	0.86	71	9.0 ± 0.3(9.3)
PNDIT-F3N	10	15.8	15.4	0.86	73	9.7 ± 0.3(10.0)
PNDIT-F3N	20	15.6	15.2	0.86	73	9.6 ± 0.2(9.8)

[a)]The average data were obtained from ten independent devices.

copolymer PTzBI-Si, generating a photocurrent as a result of the charge dissociation.[33,34]

Additionally, the incorporation of an ETL can enhance the V_{OC} since the ETL can promote the formation of an ohmic contact between the photoactive layer and the cathode; however, in our current case, the V_{OC} of the fabricated all-PSCs remains unchanged upon the incorporation of ETL. These results demonstrate that different from previously reported working mechanisms of water alcohol soluble polymers (WASPs) in fullerene-based PSCs, where interfacial dipole and/or interfacial doping played the major roles in improving the PCE.[35,36] In this work, the WASP improves the PCE of all-PSCs by participating in charge dissociation between the electron-donating polymer in the photoactive layer and n-type WASP interfacial layer. This result also indicates that the performance of all-PSCs can be further improved by the rational design of new n-type WASPs or donor-like p-type WASPs.

In addition to high PCE, device stability also plays a critical role in the practical application of PSCs. To evaluate the stability of the resulting all-PSCs, we stored these devices in a nitrogen-protected glove box with water and oxygen contents of less than 0.1 ppm. PCE versus storage time is shown in **Figure 2**, and the data are summarized in Table S1 (Supporting Information). The PCE of the control device without ETL dramatically decreased and retained only 21% of the initial PCE value after storage at 25 °C for 2000 h. Devices containing a thin layer of PEI (10 nm) exhibited slightly improved stability, with a PCE of 51% of the initial value after storing at 25 °C for 2000 h. In contrast, the device containing a thin layer of PNDIT-F3N (10 nm) as the ETL presented an obviously improved stability, which remains almost unchanged in the initial 500 h and retains nearly 90% of its initial value after storage for 2000 h. The stability of encapsulated devices under continuous illumination in air was also tested and is shown in Figure S1 (Supporting Information). A simulated sun light with intensity of 100 mW cm^{-2} was used as light source. The temperature and relative humidity of environment were kept at 25 °C and 70%. Device without ETL exhibited dramatic decrease in PCE and retained only 24% of the initial value under illumination for 250 h. Device containing a thin layer of PEI (10 nm) exhibited slightly improved stability, with a PCE of 30% of the initial value under illumination for 250 h. However, for the device with 10 nm PNDIT-F3N as ETL, obvious improvement in stability was observed, which retains 47% of its initial value under illumination for 250 h. As all of these PSCs have the same structure with a difference only in the ETL, it is reasonable to attribute the variation in device stability exclusively to the effects of the interfacial layer.

PEI has a non-conjugated backbone with only saturated chemical bonds, and all devices were stored in a N_2-protected glove box, and thus, the degradation of device performance due to the intrinsic molecular structures should be ruled out. Moreover, a reaction between the metal electrode and the ETL is also unlikely since inert Ag metal was used as the electrode. It is worth noting that the metal atom diffusion in organic light-emitting diodes (OLEDs) can largely reduce the efficiency by quenching the light emission.[37–39] Given the similar architectures of PSC and OLED devices, the interfacial failure may result from metal atom diffusion into the active layer during the device storage. For the device without ETL, the photoactive layer and metal cathode are in direct contact, and thus, the metal atoms of the cathode would diffuse into the photoactive layer at the interface to result in a decrease in stability.

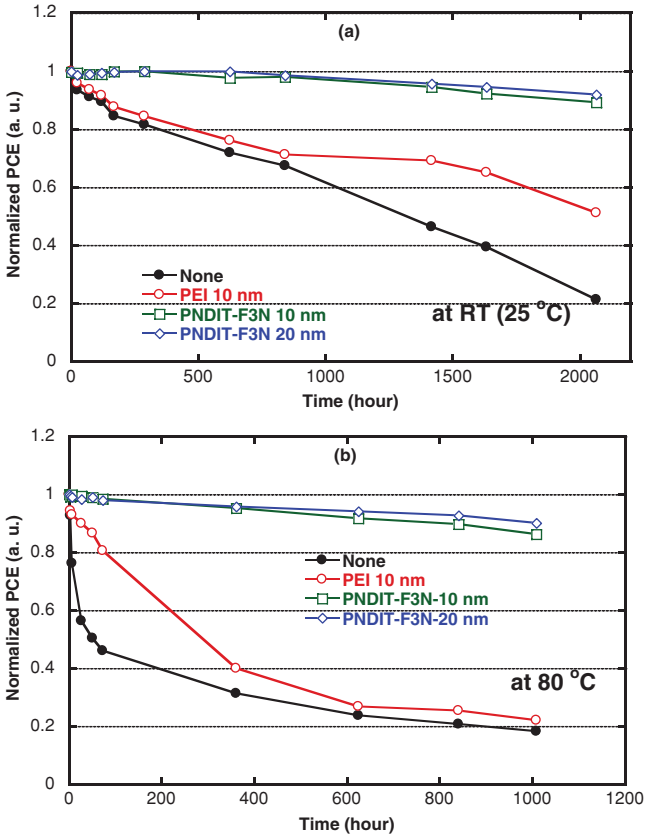

Figure 2. Stability tests of all-PSCs with different ETLs that stored in the dark at a) 25 °C and b) 80 °C.

For the device with a thin layer of PEI (thickness of ≈10 nm) as the ETL, the diffusion of the metal atoms of the cathode can be blocked by the PEI layer, thus leading to improved stability. In contrast, the stability was obviously improved for the device based on PNDIT-F3N as the ETL, which can be ascribed to effective reduction in the diffusion of the metal atoms of the cathode, since a segment of the PNDIT-F3N backbone is less likely to move than that of the nonconjugated PEI backbone. This assumption can be verified by baking these devices at 80 °C to accelerate metal diffusion. The efficiency of device containing PNDIT-F3N as the ETL slightly decreased upon thermal treatment, while the efficiency dramatically decreased for the device with PEI as the ETL and the pristine devices without ETL (Figure 2b and Table S2 in the Supporting Information). The thermal treatment activated the metal diffusion, and the PEI layer tends to melt at 80 °C since its melting point is only ≈50 °C (see the differential scanning calorimetry measurement in Figure S2, Supporting Information), thus losing the blocking ability of its metal atoms. However, thanks to the high glass-transition temperature (T_g) of PNDIT-F3N (no apparently T_g within 250 °C as shown in Figure S2, Supporting Information), the device with PNDIT-F3N as an ETL can efficiently block metal atom diffusion even at 80 °C. The same tendency was also observed in fullerene-based PSC and is shown in Figure S3 (Supporting Information), demonstrating the universality of our conclusions.

To further understand the effect of metal diffusion on the decrease in PCE, the relationship between V_{OC} and light intensity (P_{light}) was plotted and measured.[40] The slope of V_{OC} versus log P_{light} provides a relationship to the k_BT/q value (where q is the elementary charge, T is the temperature in Kelvin, and k_B is Boltzmann's constant). If the slope is close to 2 k_BT/q, the recombination mechanism is dominated by monomolecular and/or trap-assisted recombination, otherwise bimolecular recombination occurs in devices when the slope is close to k_BT/q.[41,42] As shown in **Figure 3**a, the slopes of fresh all-PSC with PNDIT-F3N (1.13 k_BT/q) or without PNDIT-F3N (1.20 k_BT/q) as the ETL are far from 2 k_BT/q and close to k_BT/q, demonstrating bimolecular recombination plays a dominant role in this system and less monomolecular and/or trap-assisted recombination occurs in fresh devices since metal diffusion is not obvious. After thermal annealing at 80 °C for 100 h, the slope for the device with PNDIT-F3N as the ETL slightly increased to 1.23 k_BT/q. However, the slope for the device without an ETL increased to 1.66 k_BT/q, demonstrating that the recombination mechanism transforms to monomolecular

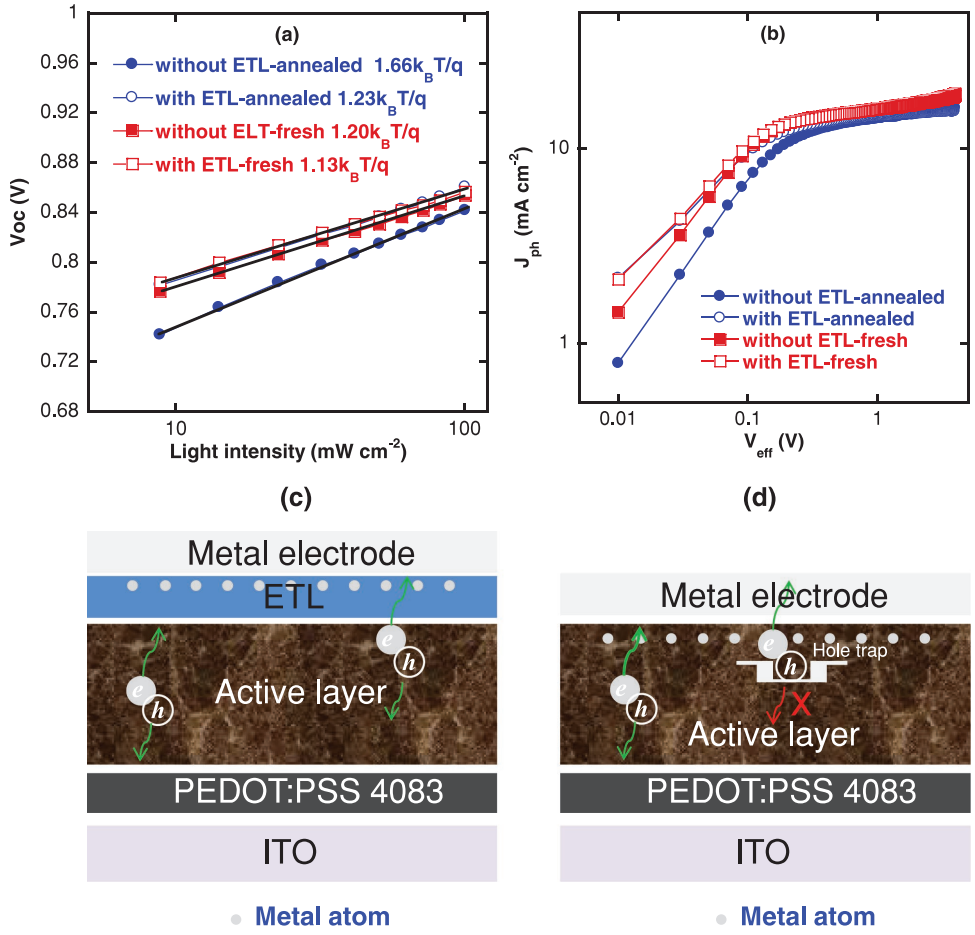

Figure 3. a) V_{OC} versus light intensity and b) photocurrent density (J_{ph}) versus effective voltage (V_{eff}) characteristics of fresh and annealed (@ 80 °C for 100 h) all-PSCs with or without PNDIT-F3N as an ETL. c,d) Illustrations of metal diffusion in devices with (c) or without (d) an ETL, respectively.

and/or trap-assisted recombination in this device, which can be ascribed to diffused metal atoms acting as trap sites (more specifically hole traps) in the active layer (as depicted in Figure 3c,d). The photocurrent density (J_{ph}) versus the effective voltage (V_{eff}) of the all-PSC was determined to obtain the charge extraction efficiency in these devices.[43,44] As shown in Figure 3b, for the devices with PNDIT-F3N as an ETL, both fresh and annealed devices have nearly identical curves, demonstrating that the charge extraction efficiency is unchanged, even after 100 h of thermal annealing at 80 °C. However, for devices without an ETL, the charge extraction efficiency decreases greatly after thermal annealing at 80 °C for 100 h, indicating that diffused metal atoms hindered charge extraction.

Metal atom diffusion can dramatically decrease the stability of PSCs and has been widely reported in OLEDs, but less attention has been paid to metal atom diffusion in PSCs. Our results will hopefully draw attention to this field and provide a new guide for designing efficient and stable ETL materials. Moreover, considering that thick ETLs block metal atom diffusion may further improve the stability of PSCs, we thus tried to increase the thickness of PEI from 10 to 20 nm; however, the device showed nearly no *J*–*V* characteristics. This observation can be understood as the fact that PEI is a completely insulating material, the incorporation of 20 nm of PEI would introduce a very large series resistance in the interconnecting layer (ICL), and therefore, electrons would be unable to move from the active layer through the PEI layer to the electrode. In fact, in single-junction cells, the optimal thickness of PEI is precisely controlled within 10 nm.[31] In contrast, PNDIT-F3N can be applied to produce high-performance devices in a wide range of thicknesses owing to the good electron transport property of the backbone.[45] Thus, 20 nm PNDIT-F3N was used as an ETL in all-PSCs. The resulting device retained a high PCE of 9.8% with a J_{SC} of 15.6 mA cm^{-2}, a V_{OC} of 0.86 V, and an FF of 73%. More importantly, increasing the thickness of PNDIT-F3N from 10 to 20 nm did not lead to a dramatic decrease in the PCE but improved the stability, and the devices retained 92% of their initial PCE after storage at 25 °C for 2000 h and retained 90% of their initial PCE after storage at 80 °C for 1000 h (Figure 2), which demonstrated that using a thicker ETL can effectively improve device stability. Although further increase in the thickness of PNDIT-F3N to 50 nm led to a further improved stability, the initial PCE decreased from 10% to 9.1%. To overcome this trade-off, we fabricated a homotandem device to simultaneously achieve a high PCE and retain stability.

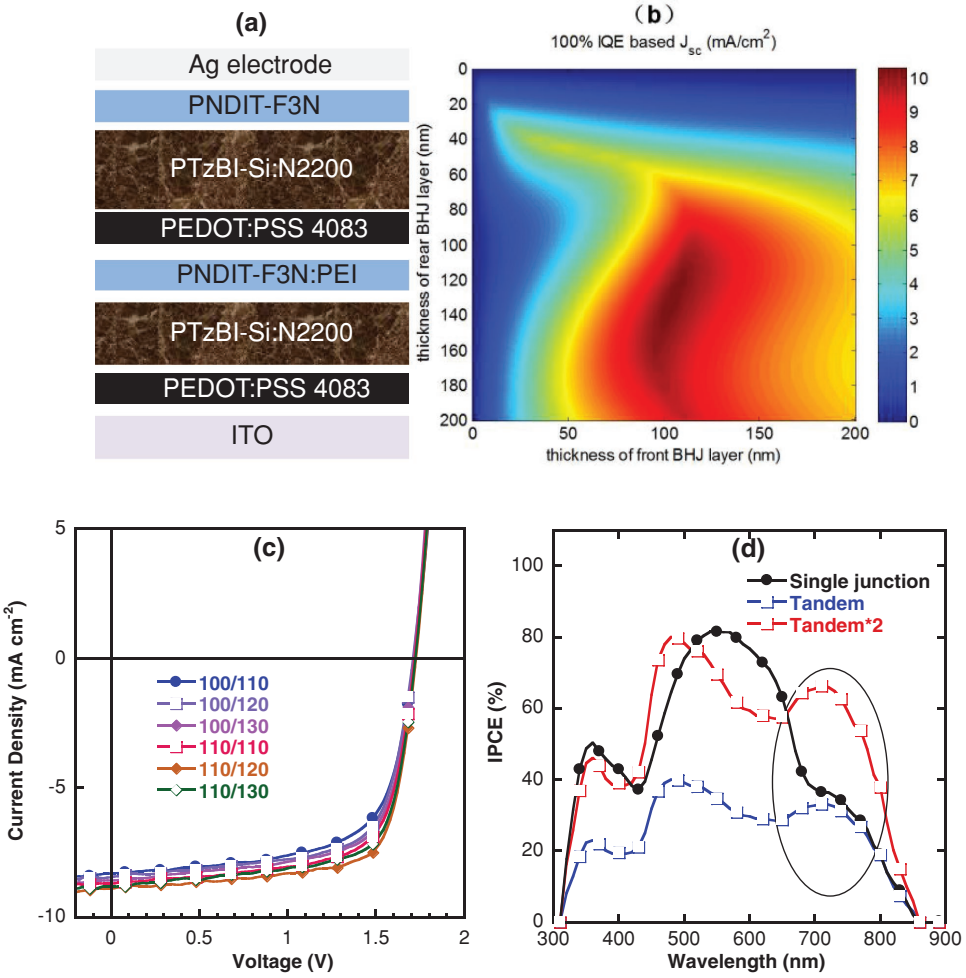

Figure 4. a) Tandem all-PSC device structure. b) Simulated J_{sc} generated in conventional double-junction tandem all-PSCs as a function of the thickness of the front and back cells. c) *J*–*V* characteristics of tandem all-PSCs with various thicknesses of the front and back cells. d) EQE spectra of single-junction and tandem all-PSCs.

Table 2. Device data for tandem all-PSCs with various thicknesses of the front and back cells.

Sub-cell thickness [nm] Front/back	Simulated J_{sc} [mA cm^{-2}]	Measured J_{sc} [mA cm^{-2}]	Integrated J_{sc} [mA cm^{-2}]	V_{oc} [V]	FF [%]	PCE [avg[a]/max] [%]
100/110	9.2	8.3	/	1.72	65	9.1 ± 0.2(9.3)
100/120	9.7	8.5	/	1.72	67	9.6 ± 0.2(9.8)
100/130	10.1	8.6	/	1.72	68	9.8 ± 0.3(10.1)
110/110	10.1	8.7	/	1.72	69	9.7 ± 0.2(9.9)
110/120	10.2	8.9	8.6	1.72	72	10.9 ± 0.3(11.2)
110/130	10.1	8.8	/	1.72	70	10.4 ± 0.2(10.6)

[a]The average data were obtained from ten independent devices.

Creating a tandem device structure is considered a promising approach to improve PSC performance by tackling the main losses in single-junction PSCs. Another striking advantage of tandem structure PSC is that it exhibits a relatively low photocurrent and thus is favorable for achieving efficient large area module PSCs, since the power loss on the series resistance in large area electrode will be obviously suppressed due to the lower photocurrent. Typically, a tandem solar cell consists of a front cell and a back cell connected by an ICL,[46,47] where the front cell is hidden from the metal electrode by the back cell and is therefore less likely to be affected by metal atom diffusion, and the stability is expected to improve. Homojunction tandem devices with the configuration of ITO/PEDOT/PSTzBI-Si:N2200/PNDIT-F3N:PEI/PEDOT/PSTzBI-Si:N2200/PNDIT-F3N/Ag were fabricated (shown in **Figure 4**a), where the PNDIT-F3N:PEI/PEDOT served as the ICL to facilitate charge transport.[48] Optical analysis of the tandem PSCs using the transfer matrix modeling method was performed to provide a guideline on the best device architecture.[49] According to the simulation result (Figure 4b), the optimal thicknesses of the front and back cells are 110 and 120 nm, respectively, with a maximum J_{SC} of 10.2 mA cm^{-2}. To verify the simulated and experimental results, we fabricated devices with an increase in both the front cell and back cell thicknesses from 100 to 130 nm. Figure 4c and **Table 2** show that the experimental data match very well with the simulated results. When the thicknesses of the front cell and back cell are 110 and 120 nm, respectively, the J_{SC} achieves a maximum value of 8.9 mA cm^{-2}, with a corresponding V_{OC} of 1.72 V and an FF of 72%. The V_{OC} is the sum of individual sub-cells indicating that these two sub-cells are successfully connected in series. More importantly, FF reaches as high as 72%, which is the highest value in tandem PSCs with a solution-processed ICL, implying that the generated charges are efficiently recombined in the ICL. Finally, the resulting device achieved the best PCE of 11.2% under the optimal conditions, which is, to the best of our knowledge, the highest value achieved so far for all-polymer tandem solar cells.

Notably, these measured J_{SC} values can be verified by the EQE curves in Figure 4d, here $EQE_{tandem} \times 2$ was used to estimate the total number of photons being converted to electrons in tandem cell, which are often seen in reported homojunction tandem devices.[50,51] It can be seen that there is an apparent increase within the range of 700–850 nm when comparing the EQE_{single} junction and $EQE_{tandem} \times 2$, indicating that more photons are utilized by the tandem device, particularly in the range of 700–850 nm. The integrated J_{SC} of the tandem cell reached 8.6 mA cm^{-2}. These data are consistent with the J_{SC} of tandem devices measured under AM 1.5G, confirming the reliability of the measured J_{SC}. Moreover, the stability of tandem all-PSC at room temperature and annealed at 80 °C was tested. As shown in **Figure 5**, the devices retained 94% of their initial value after storage at 25 °C for 2000 h and retained 93% of their initial PCE after storage at 80 °C for 1000 h (Table S3, Supporting Information), which are better than those of single-junction all-PSCs, thus demonstrating that the tandem structure can be an efficient way to improve the device performance and stability.

In conclusion, we developed all-polymer solar cells with simultaneously improved efficiency and stability, and realized that the interfacial stability played a crucial role in determining the stability of PSCs. One main pathway of interfacial failure results from thermally deposited metal electrode atoms diffusing into the active layer and hinder the charge generation and collection. Of particular importance is that the diffusion of metal atoms can be slowed down and even blocked by using thicker interlayer materials and/or high-glass-transition-temperature interlayer materials. Additionally, using a tandem device structure, where the front cell is separated

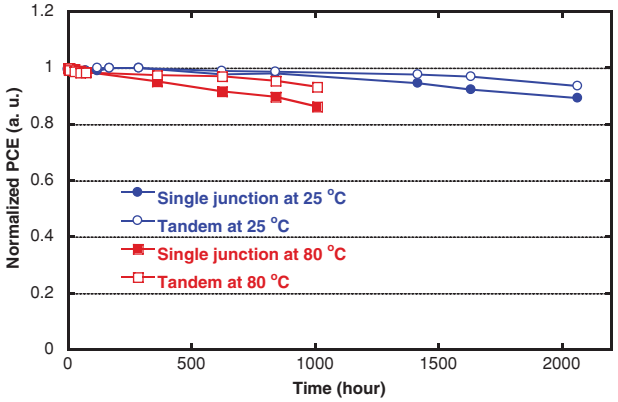

Figure 5. Stability tests of tandem all-PSCs stored in the dark at 25 °C and 80 °C. The stability data of single-junction are also included as comparisons.

from the metal electrode by the back cell, is also an efficient way to improve both the device performance and the device stability. These findings demonstrated that the tandem PSC structure is a potential candidate for future module design since it offers a new approach to improve both the PCE and the stability of the PSC device. Our results pave a new way for designing efficient ETL materials for high-performance, stable all-PSC fabrication.

Experimental Section

All-PSC Fabrication: ITO-coated glass substrates were successively precleaned with detergent, acetone, de-ionized water, and isopropanol. After being baked at 60 °C for more than 2 h, 40 nm PEDOT:PSS (Clevios P VP AI4083) was spin-coated onto the ITO substrate and baked at 150 °C for 20 min. Then, the substrates were transferred into a nitrogen-protected glove box. The PTzBI-Si:N2200 active layer (1:0.5 w/w) was formed by spin-coating from its solution with 2-methyltetrahydrofuran solvent, and film thicknesses of 100–150 nm were created by adjusting the solution concentration and spin speed (the details of active layer processing condition are summarized in Table S4 of the Supporting Information). Then, the active layers were baked at 120 °C for 10 min. Next, 10 nm of PEI or 10–20 nm of PNDIT-F3N was spin-coated onto the active layers with the solvent of methanol. The devices were finished by evaporating 100 nm of Ag through a shadow mask in a vacuum chamber with a base pressure of 1×10^{-7} mbar.

Tandem All-PSC Fabrication: First, 40 nm of PEDOT:PSS (Clevios P VP AI4083) was spin-coated onto ITO substrates and baked at 150 °C for 20 min. Then, PTzBI-Si:N2200 active layers (1:0.5 w/w) were spin-coated onto PEDOT:PSS to achieve films with thicknesses of 100–110 nm and were baked at 120 °C for 10 min in a nitrogen-protected glove box. Next, 20 nm of PNDIT-F3N:PEI with a blend ratio of (7:3) was spin-coated onto PTzBI-Si:N2200, and subsequently PEDOT:PSS was spin-coated onto the PNDIT-F3N:PEI blend film in an ambient atmosphere and stored in low vacuum (100 Pa) for 30 min to remove residual water. Then, 110–130 nm of a PTzBI-Si:N2200 active layer was spin-coated onto PEDOT:PSS and baked at 120 °C for 10 min to complete the thermal annealing process. Subsequently, 10 nm of PNDIT-F3N was spin-coated onto PTzBI-Si:N2200. Devices were finished by evaporating 100 nm of Ag through a shadow mask (5.16 mm^2) in a vacuum chamber with a base pressure of 1×10^{-7} mbar.

Device Characterization: The *J–V* curves were measured on a computer-controlled Keithley 2400 sourcemeter under 1 sun, AM 1.5 G spectrum from a class solar simulator (Taiwan, Enlitech); the light intensity was 100 mW cm^{-2}, as calibrated by a China General Certification Center certified reference monocrystal silicon cell (Enlitech). Before the *J–V* test, a physical mask with an aperture with precise area of 4 mm^2 was used to define the device area. The EQE spectra were performed on a commercial EQE measurement system (Taiwan, Enlitech, QE-R3011).

Supporting Information

Supporting Information is available from the Wiley Online Library or from the author.

Acknowledgements

This work was financially supported by the Natural Science Foundation of China (Grant Nos. 21634004, 51521002, 51603070, and 91633301), the Ministry of Science and Technology (Grant No. 2014CB643501), and the Science and Technology Program of Guangzhou (Grant No. 201707020019).

Conflict of Interest

The authors declare no conflict of interest.

Keywords

all-polymer solar cell, homojunction tandem, interfacial charge dissociation, interfacial stability

Received: May 17, 2018
Revised: June 12, 2018
Published online:

[1] G. Yu, J. Gao, J. C. Hummelen, F. Wudl, A. J. Heeger, *Science* **1995**, *270*, 1789.
[2] B. Kippelen, J.-L. Bredas, *Energy Environ. Sci.* **2009**, *2*, 251.
[3] C. J. Brabec, S. Gowrisanker, J. J. M. Halls, D. Laird, S. Jia, S. P. Williams, *Adv. Mater.* **2010**, *22*, 3839.
[4] F. C. Krebs, N. Espinosa, M. Hösel, R. R. Søndergaard, M. Jørgensen, *Adv. Mater.* **2014**, *26*, 29.
[5] W. Li, L. Ye, S. Li, H. Yao, H. Ade, J. Hou, *Adv. Mater.* **2018**, *30*, 1707170.
[6] Y. Cai, L. Huo, Y. Sun, *Adv. Mater.* **2017**, *29*, 1605437.
[7] H.-J. Bin, Y.-F. Li, *Acta Polym. Sin.* **2017**, *9*, 1444.
[8] J. Huang, H. Wang, K. Yan, X. Zhang, H. Chen, C.-Z. Li, J. Yu, *Adv. Mater.* **2017**, *29*, 1606729.
[9] S. X. Li, L. L. Zhan, F. Liu, J. Ren, M. M. Shi, C. Z. Li, T. P. Russell, H. Z. Chen, *Adv. Mater.* **2018**, *30*, 1705208.
[10] K. Zhang, F. Huang, Y. Cao, *Acta Polym. Sin.* **2017**, *9*, 1400.
[11] N. Li, J. D. Perea, T. Kassar, M. Richter, T. Heumueller, G. J. Matt, Y. Hou, N. S. Güldal, H. Chen, S. Chen, S. Langner, M. Berlinghof, T. Unruh, C. J. Brabec, *Nat. Commun.* **2017**, *8*, 14541.
[12] H. Cha, J. Wu, A. Wadsworth, J. Nagitta, S. Limbu, S. Pont, Z. Li, J. Searle, M. F. Wyatt, D. Baran, J. S. Kim, I. McCulloch, J. R. Durrant, *Adv. Mater.* **2017**, *29*, 1701156.
[13] N. Gasparini, M. Salvador, S. Strohm, T. Heumueller, I. Levchuk, A. Wadsworth, J. H. Bannock, J. C. d. Mello, H. J. Egelhaaf, D. Baran, I. McCulloch, C. J. Brabec, *Adv. Energy Mater.* **2017**, *7*, 1700770.
[14] M. O. Reese, A. M. Nardes, B. L. Rupert, R. E. Larsen, D. C. Olson, M. T. Lloyd, S. E. Shaheen, D. S. Ginley, G. Rumbles, N. Kopidakis, *Adv. Funct. Mater.* **2010**, *20*, 3476.
[15] K. Norrman, M. V. Madsen, S. A. Gevorgyan, F. C. Krebs, *J. Am. Chem. Soc.* **2010**, *132*, 16883.
[16] C. Duan, K. Zhang, C. Zhong, F. Huang, Y. Cao, *Chem. Soc. Rev.* **2013**, *42*, 9071.
[17] Z. Hu, K. Zhang, F. Huang, Y. Cao, *Chem. Commun.* **2015**, *51*, 5572.
[18] Z. He, B. Xiao, F. Liu, H. Wu, Y. Yang, S. Xiao, C. Wang, T. P. Russell, Y. Cao, *Nat. Photonics* **2015**, *9*, 174.
[19] S. Feng, C. Liu, X. Xu, X. Liu, L. Zhang, Y. Nian, Y. Cao, J. Chen, *ACS Macro Lett.* **2017**, *6*, 1310.
[20] H.-H. Cho, S. Kim, T. Kim, V. G. Sree, S.-H. Jin, F. S. Kim, B. J. Kim, *Adv. Energy Mater.* **2018**, *8*, 1701436.
[21] X. Xu, Z. Li, W. Zhang, X. Meng, X. Zou, D. D. C. Rasi, W. Ma, A. Yartsev, M. R. Andersson, R. A. Janssen, E. Wang, *Adv. Energy Mater.* **2018**, *8*, 1700908.
[22] T. Kim, J. Choi, H. J. Kim, W. Lee, B. J. Kim, *Macromolecules* **2017**, *50*, 6861.
[23] T. Kim, R. Younts, W. Lee, S. Lee, K. Gundogdu, B. J. Kim, *J. Mater. Chem. A* **2017**, *5*, 22170.
[24] Y. Zhang, Y. Xu, M. J. Ford, F. Li, J. Sun, X. Ling, Y. Wang, J. Gu, J. Yuan, W. Ma, *Adv. Energy Mater.* **2018**, *8*, 1800029.

[25] Y.-Y. Yu, C.-H. Chen, C.-C. Chueh, C.-Y. Chiang, J.-H. Hsieh, C.-P. Chen, W.-C. Chen, *ACS Appl. Mater. Interfaces* **2017**, *9*, 27853.
[26] T. Kim, J.-H. Kim, T. E. Kang, C. Lee, H. Kang, M. Shin, C. Wang, B. Ma, U. Jeong, T.-S. Kim, B. J. Kim, *Nat. Commun.* **2015**, *6*, 8547.
[27] B. Fan, L. Ying, Z. Wang, B. He, X.-F. Jiang, F. Huang, Y. Cao, *Energy Environ. Sci.* **2017**, *10*, 1243.
[28] Z. G. Zhang, Y. Yang, J. Yao, L. Xue, S. Chen, X. Li, W. Morrison, C. Yang, Y. Li, *Angew. Chem., Int. Ed.* **2017**, *56*, 13503.
[29] Z. Li, X. Xu, W. Zhang, X. Meng, Z. Genene, W. Ma, W. Mammo, A. Yartsev, M. R. Andersoon, R. A. J. Janssen, E. Wang, *Energy Environ. Sci.* **2017**, *10*, 2212.
[30] B. Fan, L. Ying, P. Zhu, F. Pan, F. Liu, J. Chen, F. Huang, Y. Cao, *Adv. Mater.* **2017**, *29*, 1703906.
[31] Y. Zhou, C. Fuentes-Hernandez, J. Shim, J. Meyer, A. J. Giordano, H. Li, P. Winget, T. Papadopoulos, H. Cheun, J. Kim, M. Fenoll, A. Dindar, W. Haske, E. Najafabadi, T. M. Khan, H. Sojoudi, S. Barlow, S. Graham, J.-L. Brédas, S. R. Marder, A. Kahn, B. Kippelen, *Science* **2012**, *336*, 327.
[32] Y.-M. Chang, R. Zhu, E. Richard, C.-C. Chen, G. Li, Y. Yang, *Adv. Funct. Mater.* **2012**, *22*, 3284.
[33] C. Sun, Z. Wu, Z. Hu, J. Xiao, W. Zhao, H.-W. Li, Q.-Y. Li, S. W. Tsang, Y.-X. Xu, K. Zhang, H.-L. Yip, J. Hou, F. Huang, Y. Cao, *Energy Environ. Sci.* **2017**, *10*, 1784.
[34] S. Dong, Z. Hu, K. Zhang, Q. Yin, X. Jiang, F. Huang, Y. Cao, *Adv. Mater.* **2017**, *29*, 1701507.
[35] K. Zhang, C. Zhong, S. Liu, C. Mu, Z. Li, H. Yan, F. Huang, Y. Cao, *ACS Appl. Mater. Interfaces* **2014**, *6*, 10429.
[36] Z. He, C. Zhong, S. Su, M. Xu, H. Wu, Y. Cao, *Nat. Photonics* **2012**, *6*, 591.
[37] Y. Park, V. E. Choong, B. R. Hsieh, C. W. Tang, Y. Gao, *Phys. Rev. Lett.* **1997**, *78*, 3955.
[38] V. Choong, Y. Park, Y. Gao, T. Wehrmeister, K. Müllen, B. R. Hsieh, C. W. Tang, *Appl. Phys. Lett.* **1996**, *69*, 1492.
[39] V.-E. Choong, Y. Park, N. Shivaparan, C. W. Tang, Y. Gao, *Appl. Phys. Lett.* **1997**, *71*, 1005.
[40] S. R. Cowan, A. Roy, A. J. Heeger, *Phys. Rev. B* **2010**, *82*, 245207.
[41] M. M. Mandoc, F. B. Kooistra, J. C. Hummelen, B. d. Boer, P. W. M. Blom, *Appl. Phys. Lett.* **2007**, *91*, 263505.
[42] W. L. Leong, S. R. Cowan, A. J. Heeger, *Adv. Energy Mater.* **2011**, *1*, 517.
[43] L. Lu, T. Xu, W. Chen, E. S. Landry, L. Yu, *Nat. Photonics* **2014**, *8*, 716.
[44] K. Zhang, R. Xu, W. Ge, M. Qi, G. Zhang, Q.-H. Xu, F. Huang, Y. Cao, X. Wang, *Nano Energy* **2017**, *34*, 164.
[45] Z. Wu, C. Sun, S. Dong, X.-F. Jiang, S. Wu, H. Wu, H.-L. Yip, F. Huang, Y. Cao, *J. Am. Chem. Soc.* **2016**, *138*, 2004.
[46] N.-K. Persson, O. Inganäs, *Sol. Energy Mater. Sol. Cells* **2006**, *90*, 3491.
[47] K. Zhang, K. Gao, R. Xia, Z. Wu, C. Sun, J. Cao, L. Qian, W. Li, S. Liu, F. Huang, X. Peng, L. Ding, H.-L. Yip, Y. Cao, *Adv. Mater.* **2016**, *28*, 4817.
[48] K. Zhang, B. Fan, R. Xia, X. Liu, Z. Hu, H. Gu, S. Liu, H. L. Yip, L. Ying, F. Huang, Y. Cao, *Adv. Energy Mater.* **2018**, *8*, 1703180.
[49] A. R. b. M. Yusoff, D. Kim, H. P. Kim, F. K. Shneider, W. J. da Silva, J. Jang, *Energy Environ. Sci.* **2015**, *8*, 303.
[50] H. Zhou, Y. Zhang, C.-K. Mai, S. D. Collins, G. C. Bazan, T.-Q. Nguyen, A. J. Heeger, *Adv. Mater.* **2015**, *27*, 1767.
[51] H. Kang, S. Kee, K. Yu, J. Lee, G. Kim, J. Kim, J.-R. Kim, J. Kong, K. Lee, *Adv. Mater.* **2015**, *27*, 1408.